Acoustically targeted chemogenetics for the non-invasive control of neural circuits

Jerzy O. Szablowski [ID], Audrey Lee-Gosselin, Brian Lue, Dina Malounda and Mikhail G. Shapiro [ID]*

Neurological and psychiatric disorders are often characterized by dysfunctional neural circuits in specific regions of the brain. Existing treatment strategies, including the use of drugs and implantable brain stimulators, aim to modulate the activity of these circuits. However, they are not cell-type-specific, lack spatial targeting or require invasive procedures. Here, we report a cell-type-specific and non-invasive approach based on acoustically targeted chemogenetics that enables the modulation of neural circuits with spatiotemporal specificity. The approach uses ultrasound waves to transiently open the blood–brain barrier and transduce neurons at specific locations in the brain with virally encoded engineered G-protein-coupled receptors. The engineered neurons subsequently respond to systemically administered designer compounds to activate or inhibit their activity. In a mouse model of memory formation, the approach can modify and subsequently activate or inhibit excitatory neurons within the hippocampus, with selective control over individual brain regions. This technology overcomes some of the key limitations associated with conventional brain therapies.

Neurological and psychiatric diseases together affect over 35% of the adult population[1–3] and often involve the dysfunction of neural circuits defined by specific spatial locations and cell types[4–8]. However, conventional pharmacological treatments for such diseases act throughout the brain, leading to significant side effects. While invasive surgery is able to target specific parts of the brain for excision or electrical stimulation, it carries significant risks. Emerging therapies based on gene or cellular therapy are also typically delivered using surgical injections, often with limited spatial coverage and acting in an always-on fashion lacking temporal dose control. Here, we introduce an alternative approach to neuromodulation that delivers spatial, cell-type and temporal control without surgery. This approach—which we call acoustically targeted chemogenetics (ATAC)—achieves this performance by combining three recently developed technologies: focused ultrasound blood–brain barrier opening (FUS-BBBO) for spatial targeting, adeno-associated virus (AAV) vectors for delivery of genes to specific cell types, and engineered chemogenetic receptors for modulation of targeted neurons using orally bioavailable[9] compounds (Fig. 1a).

FUS is an established biomedical technology that takes advantage of ultrasound's ability to focus in deep tissues such as the brain with millimetre spatial precision[10–12]. FUS-BBBO combines transcranial ultrasound in the low-intensity regime with systemically administered microbubbles, whose stable cavitation in blood vessels at the ultrasound focus results in localized, temporary and reversible opening of the BBB[13,14]. This allows small molecules, proteins, nanoparticles or viral capsids[13,15–21] to enter the brain at the site of the applied ultrasound. FUS-BBBO has been used in multiple animal species[13,22,23] and is undergoing clinical testing[10]. ATAC combines FUS with replication-incompetent AAV vectors, an established method to stably transfect mammalian cells without integration into the target genome. AAVs are widely used in neuroscience research and have recently shown promise in the clinic[24–28]. When a gene of interest carried by an AAV is encoded under an appropriate promoter, the expression of this gene can be restricted to a specific class of neurons[29]. Several AAV serotypes have been delivered to the brain via FUS-BBBO[17,18,21,30]. In ATAC, the AAV vector encodes

chemogenetic receptors, a class of engineered proteins whose expression in neurons allows these cells to be controlled by systemically administered compounds[31,32] deliverable through a number of routes, including oral and intraperitoneal (i.p.) administration[33,34]. In particular, we use designer receptors exclusively activated by designer drugs (DREADDs). These proteins are modified versions of natural activatory or inhibitory G-protein-coupled receptors, engineered to respond to synthetic molecules rather than endogenous ligands[35]. Thanks to their ability to selectively control neural circuits, DREADDs are being considered for clinical translation[33].

In the ATAC paradigm, a one-time FUS-BBBO procedure 'paints' the region or regions of the brain to be modulated, while AAV vectors and DREADDs sensitize specific neurons in these regions to subsequent excitation or inhibition through administration of clozapine-N-oxide (CNO) (Fig. 1b). While the three components underlying this paradigm have been separately established, and previous work has combined AAVs with either BBBO or DREADDs, we report the integration of these three technologies to achieve ATAC's unique combination of spatial, cell-type and temporal control of neural circuits. Furthermore, we demonstrate the use of FUS-BBBO to deliver genes affecting behaviour through neuromodulation and provide fully non-invasive control of behaviour via genetically targeted neuromodulation in wild-type animals.

Here, we demonstrate the basic capabilities of ATAC in mice by evaluating the ability of this technique to selectively activate or inhibit excitatory neurons in the hippocampus and midbrain, regions involved in memory formation and volitional behaviour and implicated in several neuropathologies. Our biochemical and behavioural experiments show that ATAC enables selective neuromodulation of these parts of the brain and that inhibitory ATAC is able to reduce traumatic memory formation in a model of contextual fear learning.

Results

Anatomical and genetic targeting of DREADD expression. To evaluate the ability of ATAC to target the expression of DREADDs to a specific location in the brain, we first performed FUS-BBBO
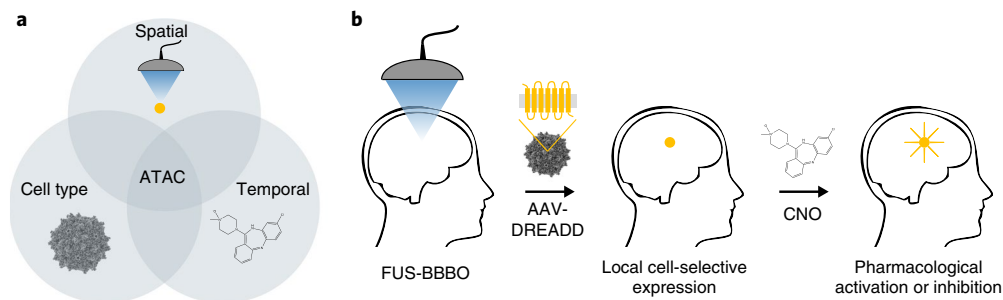

Fig. 1 | ATAC paradigm. a, The ATAC paradigm provides a combination of millimetre-precision spatial targeting using FUS, cellular specificity using viral vectors with cell-type-specific promoters driving the expression of chemogenetic receptors, and temporal control through administration of the chemogenetic ligand. **b**, In the ATAC sequence, the blood–brain barrier (BBB) is opened locally using FUS, and systemically injected AAV encoding a DREADD enters the treated area. After several weeks, the DREADD is expressed in the targeted region in cells possessing selected promoter activity. At any desired subsequent time, the DREADD-expressing neurons can be excited or inhibited through a chemogenetic drug such as CNO.
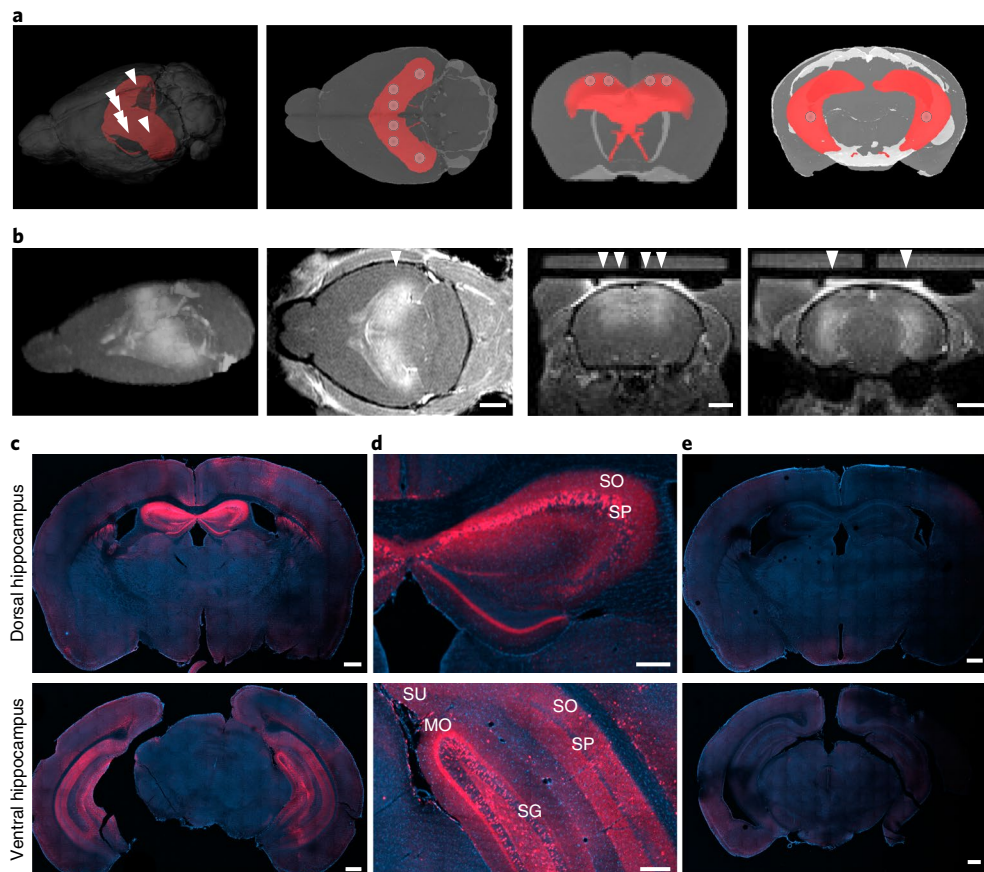

Fig. 2 | BBBO and targeted expression of DREADD in the hippocampus. a, Rendering of mouse brain with hippocampus highlighted in red and targeted locations of the centre of FUS-BBBO beams indicated with grey circles. The selected renderings are an anatomical representation of the hippocampus in the MRI images in **b**. From left to right: isometric view of the brain with arrowheads indicating targeted location of FUS-BBBO, axial view of the brain, rendered slices including dorsal and then ventral hippocampus with circles indicating the centre of a FUS beam used for BBB opening. **b**, Images from a representative T_1-weighted MRI scan acquired immediately after FUS-BBBO, with brighter areas indicating relaxation enhancement from ProHance extravasation, as shown by the arrowheads. Representative of $n = 24$ mice analysed. Scale bars, 2 mm. **c**, Representative brain sections from a single animal showing dorsal (top) and ventral (bottom) hippocampus immunostained for hM4Di-mCherry (red) six weeks after FUS-BBBO and injection of AAV9 encoding this hM4Di-mCherry under the CaMKIIa promoter. The DAPI stain demarcates cell nuclei (blue). Representative of $n = 4$ independent brains analysed. Scale bars, 500 μm. **d**, Magnified view of dorsal (top) and ventral (bottom) hippocampus showing widespread expression in molecular layers (MO) of the dentate gyrus, stratum oriens (SO), subiculum (SU), granular (SG) and pyramidal cell layers of the hippocampus (SP). Representative of $n = 4$ independent brains analysed. Scale bars, 200 μm. **e**, Representative immunostaining result for hM4Di-mCherry in a mouse that received the same viral construct, but did not undergo FUS-BBBO. Representative of $n = 3$ independent brains analysed. Scale bars, 500 μm.

on the hippocampus of wild-type mice. The hippocampus is implicated in a number of neurological and psychiatric disorders such as anxiety, epilepsy and Alzheimer's disease[36]. To achieve expression

throughout this brain structure, we performed FUS-BBBO at six locations covering the ventral and dorsal hippocampus using an FUS instrument operating at 1.5 MHz guided by magnetic resonance
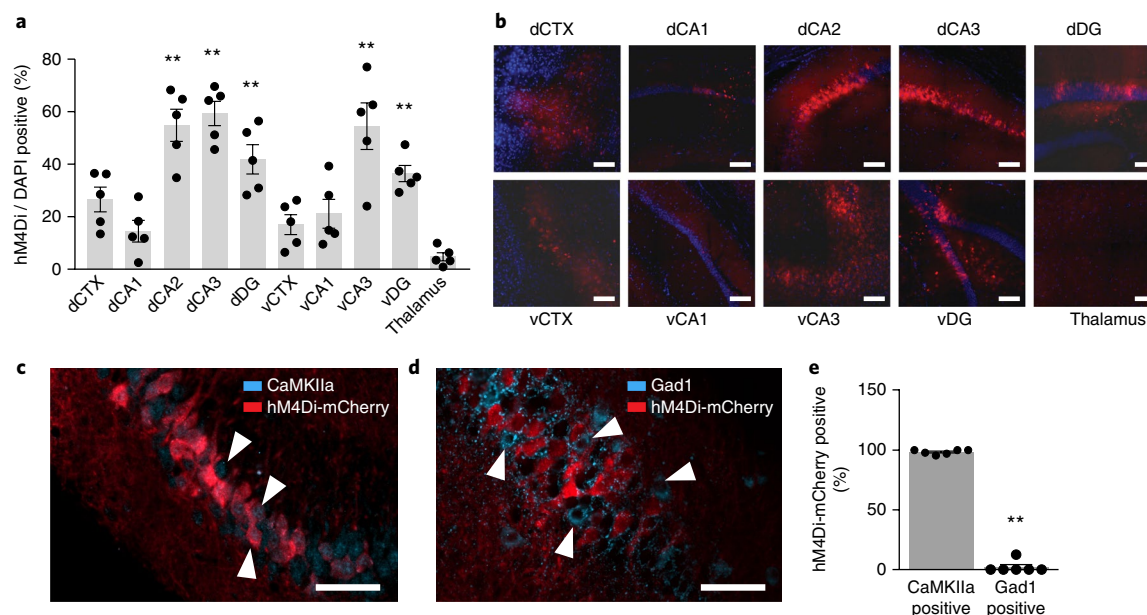
Fig. 3 | Spatial and cell-type specificity of DREADD expression. a, Percentage of cell bodies with detectable mCherry fluorescence in pyramidal layers of the hippocampus and overlaying FUS-targeted cortex (CTX), and thalamus as an untargeted negative control. These values indicate relative transduction efficiency in different fields of the hippocampus. DG, dentate gyrus; v and d, ventral and dorsal sites, respectively. $n = 5$ mice; one-way analysis of variance test compared with thalamus, variance ratio $F_{(9,40)} = 13.89$; $P = 8.7 \times 10^{-10}$; **$P < 0.01$ in comparison with negative control (thalamus), using a Tukey honestly significant difference post hoc test. Exact P values for each group are in Supplementary Table 1. **b**, Representative images of mCherry fluorescence (red) in each field. The DAPI stain (blue) marks cell nuclei. Representative of $n = 6$ mice. Scale bars, 100 μm. **c**, Representative co-immunostaining for hM4Di-mCherry and CaMKIIa. Arrowheads indicate cells positive for CaMKIIa. Representative of $n = 6$ mice. Scale bar, 50 μm. **d**, Representative co-immunostaining for hM4Di-mCherry and Gad1. Arrowheads indicate cells positive for Gad1. Scale bar, 50 μm. **e**, Percentage of DREADD-expressing cells in the CA2 region that are positively stained for CaMKIIa or Gad1, representing excitatory and inhibitory cells, respectively. $n = 6$ mice; $P = 4.75 \times 10^{-9}$, two-tailed t-test assuming unequal variance; **$P < 0.01$. Bar graphs in **a,e** represent mean ± s.e.m.

imaging (MRI) (Fig. 2a). FUS was applied immediately after an intravenous (i.v.) injection of microbubbles and viral vector, with a gadolinium contrast agent coadministered to visualize regions with successful BBBO (Fig. 2b). As our viral vector, we chose AAV9, a serotype of AAV with favourable tropism for neurons and large spatial spread after direct intracranial delivery[37]. This vector encoded the inhibitory DREADD receptor hM4Di, fused to the fluorescent reporter mCherry to facilitate histological visualization. This gene was encoded downstream of a calcium/calmodulin-dependent protein kinase II alpha (CaMKIIa) promoter, which was used to target ATAC specifically to excitatory neurons[38].

After allowing 6–8 weeks for transgene expression, the targeted locations showed widespread hM4Di expression in histological sections, covering most hippocampal regions and a small segment of cortex above the dorsal hippocampus (Fig. 2c). Expression was especially strong in the molecular and polymorph layers of dentate gyrus, the stratum oriens and stratum radiatum of the CA1, CA2 and CA3 fields, as well as the pyramidal cells of the dentate gyrus, CA2 and CA3 (Fig. 2d). Expression was present broadly throughout the hippocampus (Supplementary Fig. 1). By comparison, mice that received an i.v. injection of the same AAV9 vector without FUS-BBBO showed essentially no fluorescent signal in these brain regions (Fig. 2e), confirming that BBBO was required for gene delivery at the viral dose used in this study. To assess the possibility of off-target expression in the peripheral nervous system, we performed immunostaining against hM4Di-mCherry in dorsal root ganglia (DRG). We found no expression of DREADDs in DRG (Supplementary Fig. 2), consistent with another study showing poor efficiency of peripheral nerve transduction with AAV9[39].

A quantitative comparison of expression in FUS-targeted areas across five mice was performed using mCherry fluorescence in cell

bodies of granular cell layers, which allowed for a direct comparison of transfection efficiency between hippocampal regions. Our analysis showed that more than 50% of the cells in dorsal and ventral CA3 and dorsal CA2 were successfully transfected, and that ventral and dorsal dentate gyrus contained 42% and 36% positive cell bodies, respectively (Fig. 3a,b). The cortex and CA1 typically had lower transfection efficiencies, suggesting that these regions are less susceptible to transfection after BBBO than other hippocampal fields. As a representative non-targeted region, we looked for expression in the thalamus, which was shown in previous studies to be particularly susceptible to transfection following systemic delivery of AAV9[40], and found no significant expression (<5%, Fig. 3a,b). Full results of the statistical tests can be found in Supplementary Table 1. When compared with a direct intracranial injection of the same genetic construct using established protocols[41], the percentage of mCherry-positive cell bodies at the sites of injection was similar to regions strongly expressing the construct after FUS-BBBO (52.8 ± 10.1%, $n = 4$ mice and eight injections analysed; Supplementary Fig. 3).

To evaluate the cellular specificity of genetic targeting, we compared expression of DREADDs in cells staining positively for CaMKIIa or glutamic acid decarboxylase (Gad) 1, which serve as labels of excitatory and inhibitory neurons, respectively (Fig. 3c,d). We found that 98.4 ± 0.8% of the cells expressing the DREADD receptor also stained positively for CaMKIIa, while only 2.08 ± 2.08% of these cells co-stained for Gad1, confirming selective targeting of our constructs to excitatory neurons ($n = 6$, $P = 4.75 \times 10^{-9}$, heteroscedastic two-tailed t-test; Fig. 3e).

Targeted stimulation of the hippocampus. Depending on the DREADD encoded in the AAV vector, ATAC can be used to either stimulate or inhibit targeted neurons. To first assess the ability of

this technique to provide cell-specific activation, we targeted AAV9 carrying the excitatory DREADD hM3Dq fused to mCherry, under the CaMKIIa promoter, to the dorsal hippocampus using four FUS-BBBO sites. After allowing time for expression, we administered CNO i.p., and 2.5 h later perfused the mice to histologically monitor the expression of the activity-dependent gene product c-Fos in the dorsal CA3 region of the hippocampus (Fig. 4a). We found that cells positive for hM3Dq expression were 5.8 times more likely to exhibit c-Fos staining than cells not expressing hM3Dq (Fig. 4b,c, $n = 6$, $P = 7.1 \times 10^{-4}$, two-tailed paired t-test), indicating that systemic chemogenetic treatment allows ATAC-targeted neurons to be selectively activated several weeks after the spatial targeting procedure.

Targeted inhibition of the hippocampus and effect on memory formation. To assess the ability of ATAC to inhibit targeted neurons, and to test the functionality of this technology in a behavioural paradigm, we used FUS-BBBO to target inhibitory DREADDs (hM4Di) to the ventral and dorsal hippocampus (Fig. 5a), and assessed the impact of CNO administration on the formation of contextual fear memories. This well-established behavioural paradigm has been used in studies of anxiety, phobias, post-traumatic stress disorder and fear circuitry[42,43]. Fear conditioning has also served as a testing ground for other neuromodulatory techniques[41,44]. Since the hippocampus plays an essential role in memory formation, we hypothesized that inhibiting it non-invasively using the ATAC strategy would reduce the ability of mice to form fear memories.

Coverage of the hippocampus was achieved with FUS-BBBO applied to six sites (Fig. 2), accompanied by i.v. administration of AAV9 containing hM4Di-mCherry under the CaMKIIa promoter, to obtain ATAC mice. Two groups of control mice either were completely untreated or received i.v. virus without FUS-BBBO. After 6–8 weeks, the mice underwent a fear conditioning protocol (Fig. 5a). In this protocol, the mice were placed in a unique environment (defined by chamber shape, lighting, smell and sound; context A in Fig. 5a) while receiving three electric foot shocks, causing them to associate this environment with the noxious stimulus in a process known as contextual fear conditioning. Forty to sixty minutes before undergoing this protocol, each group of mice received injections of either CNO or saline to test the ability of targeted inhibition of ATAC-treated hippocampal neurons to reduce fear formation.

Twenty-four hours after conditioning, contextual fear recall was tested by placing mice in the same context and measuring freezing, an indication of fear[45] (Fig. 5a). ATAC mice treated with saline during conditioning froze 53.2% of the time, indicating robust fear recall. By contrast, ATAC mice that received CNO before conditioning froze only 21.8% of the time—a more than twofold reduction in fear memory ($P = 1.9 \times 10^{-5}$, $n = 13$ and $n = 7$, heteroscedastic two-tailed t-test; Fig. 5b). Comparing these two FUS-treated conditions allowed us to evaluate the efficacy of ATAC while accounting for any potential behavioural effects caused by the FUS treatment itself[46,47]. Additional controls showed that the activation of any DREADDs potentially expressed outside FUS-targeted brain regions (after a systemic AAV9 injection, but in the absence of FUS-BBBO), or CNO treatment alone in wild-type mice, did not result in a reduction in contextual fear relative to untreated controls (Fig. 5c,d). To confirm that the effect of activation of DREADDs was specific to fear formation and did not affect basic exploratory behaviour, we monitored treated and untreated mice in an open field test. One day after fear conditioning, the mice were placed in a novel environment (context B in Fig. 5a), which they were allowed to explore freely for 3 min. The exploratory behaviour of all groups of mice was unaffected by CNO administration (Fig. 5e–g).

To confirm that the effect of ATAC treatment was specific to inhibiting memory formation as opposed to sensation of stimuli such as pain, we paired each foot shock with an audible tone to
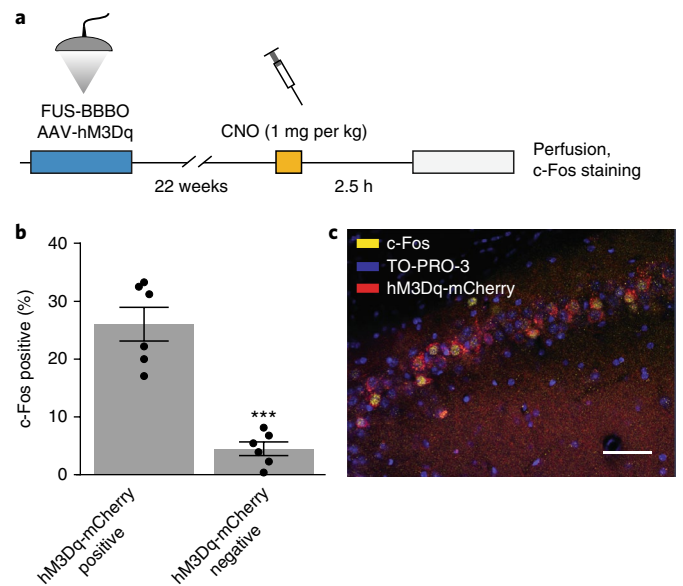
Fig. 4 | ATAC with excitatory DREADDs results in neuronal activation. **a**, Excitatory DREADD activation protocol. FUS-BBBO and an i.v. injection of AAVs was followed by a period of expression, and an i.p. injection of CNO in saline (1 mg per kg). After 2.5 h, mice were perfused, and their brains were extracted for histological evaluation. **b**, Fraction of cells in the CA3 field of the hippocampus staining positively for c-Fos after CNO administration, as a function of whether the cells are positive or negative for hM3Dq-mCherry. $P = 7.1 \times 10^{-4}$, two-tailed t-test, assuming unequal variance, $n = 6$ independently targeted hemispheres in $n = 3$ mice; ***$P < 0.001$. Bars represent mean ± s.e.m. **c**, Representative immunohistology image of CA3 with c-Fos (yellow), hM3Dq-mCherry (red) and nucleus (TO-PRO-3; blue) staining. $n = 6$ independently targeted hemispheres analysed from $n = 3$ mice. Scale bar, 50 μm.

produce an association between the tone and the shock in a process known as cued conditioning (Supplementary Fig. 4a). This process took place immediately during training and was not expected to be affected by inhibition of memory-forming regions of the hippocampus[41]. As expected, cued freezing measured at the end of the training session was unaffected by CNO treatment (Supplementary Fig. 4b–d), indicating that ATAC-treated mice were not compromised in their ability to experience salient sensory stimuli.

Intersectional ATAC in transgenic animals. In addition to its potential therapeutic applications, ATAC may facilitate the study of neurological and psychiatric disease mechanisms in animal models by allowing the modulation of disease-related spatially defined neural circuits without surgery. A complementary resource for such studies is the large number of transgenic mouse and rat lines available with cell-type-specific expression of the Cre recombinase. The delivery of a viral vector encoding any gene of interest in a Cre-dependent configuration allows the expression of this gene to be confined to the Cre-expressing cells in that animal[29]. To test whether ATAC could be used in combination with a Cre mouse line to provide non-invasive spatial and cell-type targeting of neuromodulation, we used FUS-BBBO to deliver a Cre-dependent DREADD construct into tyrosine hydroxylase / Cre (TH-Cre) transgenic mice[48]. These animals express the Cre recombinase in tyrosine-hydroxylase-positive dopaminergic neurons in the midbrain, especially in the substantia nigra pars compacta (SNc) and the ventral tegmental area (VTA). These regions are researched extensively in models of Parkinson's disease[49], addiction and reward[50] and have previously been used to validate new neuromodulation techniques[51]. Due to
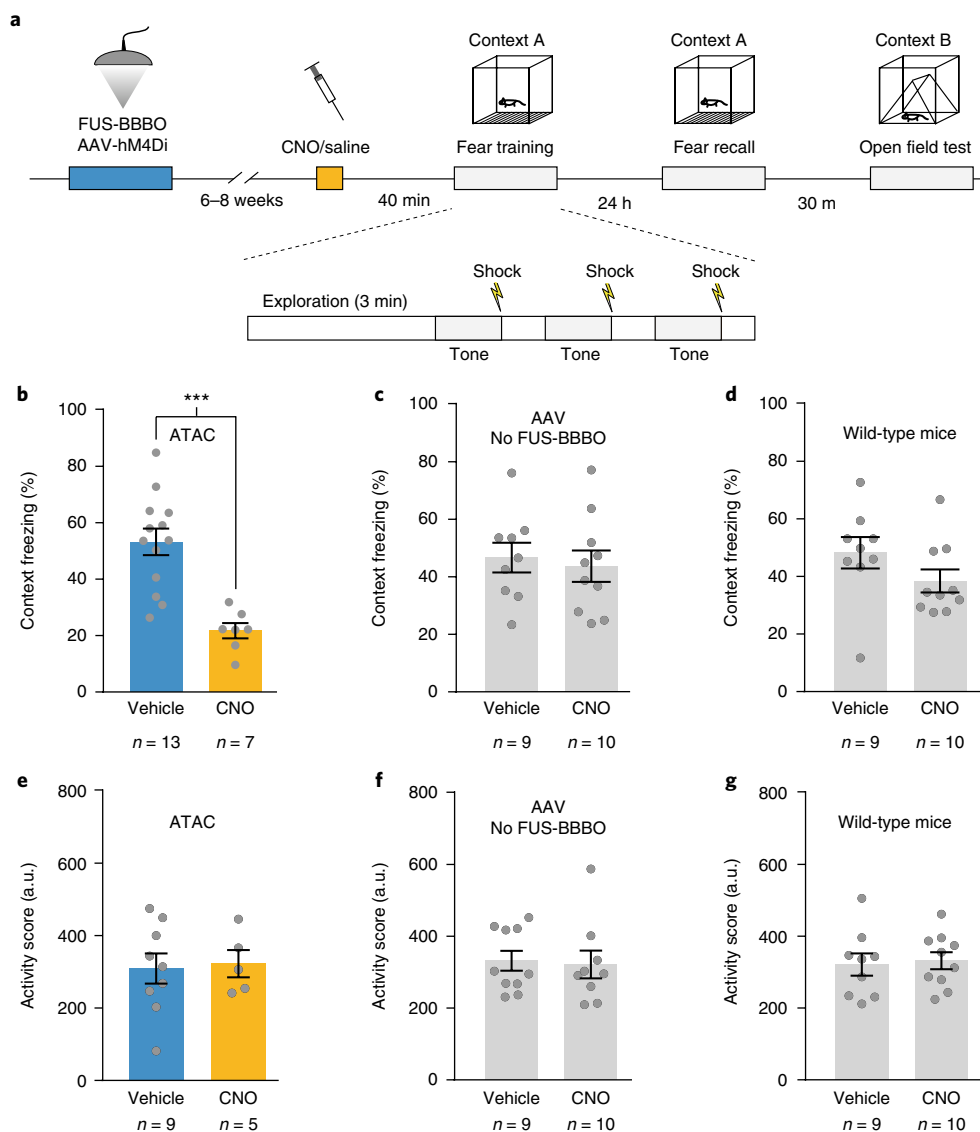
Fig. 5 | Inhibition of fear memory formation using ATAC. a, Illustration of the ATAC and fear conditioning protocol. Six to eight weeks after FUS-BBBO and administration of AAV-DREADD (hM4Di-mCherry), mice were injected with CNO or saline, then placed in a fear conditioning chamber with an electrified floor. After 3 min of free exploration, the mice received 3×30 s tones (80 dB) paired with an electric shock during the last 2 s of the tone (0.7 mA). The interval between tones was 1 min. Twenty-four hours after training, the mice were placed in the same chamber and allowed to explore for 8 min 40 s. After 30 min, the mice were placed in a different context for an open field test for 3 min. **b**, Percentage of time spent freezing in the fear recall context (context A) for ATAC mice treated with CNO or saline ($P = 1.9 \times 10^{-5}$, two-tailed heteroscedastic t-test; ***$P < 0.001$). **c**, Percentage of time spent freezing in the fear recall context (context A) for mice that received i.v. injection of AAV-DREADD without FUS-BBBO, with CNO and saline treatment (no effect found, $P = 0.69$, two-tailed heteroscedastic t-test). **d**, Percentage of time spent freezing in the fear recall context (context A) for wild-type mice treated with CNO or saline (no effect found, $P = 0.17$, two-tailed heteroscedastic t-test). **e**, Exploratory activity score in the non-fear context (context B) for ATAC mice treated with CNO or saline ($P = 0.81$, two-tailed heteroscedastic t-test). **f**, Exploratory activity score in the non-fear context (context B) for mice that received i.v. injection of AAV-DREADD without FUS-BBBO, with CNO or saline treatment (no effect found, $P = 0.65$, two-tailed Mann–Whitney test used due to non-normal distribution of data points). **g**, Exploratory activity score in the non-fear context (context B) for wild-type mice that received CNO or saline treatment (no effect found, $P = 0.79$, two-tailed heteroscedastic t-test). All bar graphs represent mean ± s.e.m. The n values under each bar indicate the number of mice tested in that experimental condition. a.u., arbitrary units.

their locations deep within the brain and their small size, surgical access to these sites is difficult, and a non-invasive approach could reduce surgical damage along the needle tract while providing spatial selectivity.

To establish the feasibility of intersectional ATAC in a Cre mouse line, we used FUS-BBBO to spatially target a Cre-dependent[52] double-floxed inverted open reading frame (DIO) hM3Dq gene fused to mCherry, under the human Synapsin-1 promoter (DIO-Syn1-hM3Dq-mCherry), encoded in AAV9 to the midbrain on a

single side of the brain (Fig. 6a), then tested our ability to activate TH-positive neurons in this region with CNO by imaging c-Fos accumulation (Fig. 6b). FUS-BBBO applied to the midbrain resulted in a BBBO that partially overlapped with the expected location of the SNc/VTA (Fig. 6c). Subsequent immunofluorescent imaging of brain sections revealed hM3Dq was present in the SNc/VTA at the FUS-BBBO site (Fig. 6d,e) and not at the contralateral site or in the DRG (Supplementary Fig. 5). We then tested the functionality of our DREADD receptor by staining for c-Fos-positive nuclei at the
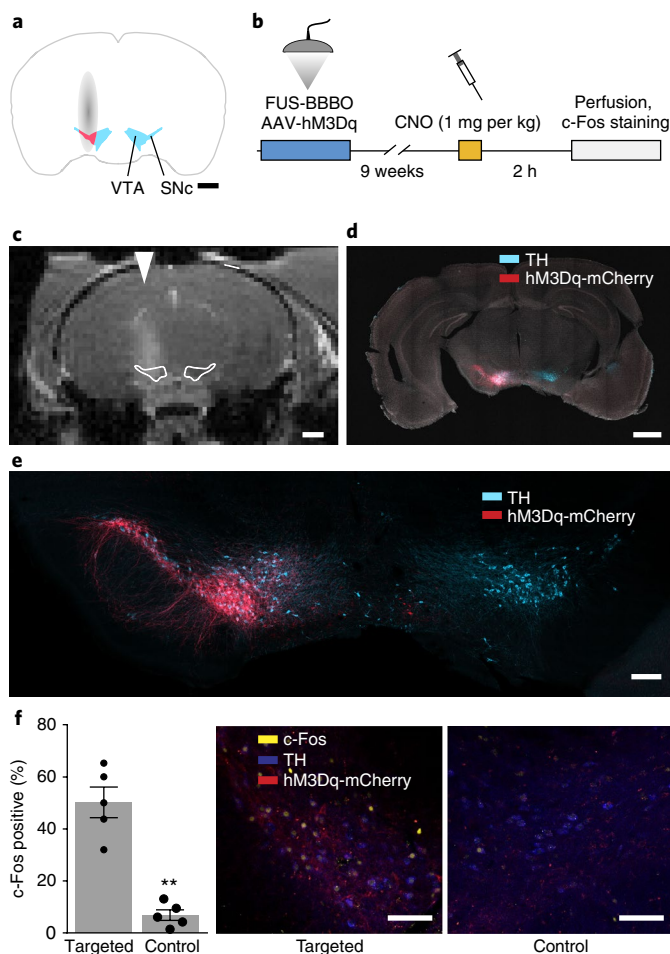
Fig. 6 | Intersectional ATAC in the midbrain of Cre transgenic mice.
a, Illustration of intersectional attack experiment. FUS-BBBO (grey) was used to target AAV encoding DIO-Syn1-hM3Dq-mCherry unilaterally to the midbrain of TH-Cre mice. Approximate locations of the TH-positive SNc/VTA and FUS target region are shown in cyan and pink, respectively. Scale bar, 1 mm. **b**, Protocol for c-Fos induction. After a period of expression, mice received an i.p. injection of CNO (1 mg per kg), and 2 h later were perfused and their brains extracted for histological evaluation. **c**, Representative T_1-weighted MRI scan indicating the site of the BBBO (representative of seven mice). Outlines show the approximate location of SNc/VTA. The arrowhead indicates the lateral targeting of FUS. Scale bar, 1 mm. **d**, Immunostaining for hM3Dq-mCherry (red) and TH (blue), counterstained with DAPI (white). Five mice were evaluated with similar results. Scale bar, 1 mm. **e**, Magnified view of SNc/VTA in **d**. Scale bar, 200 μm. **f**, Quantification of activated (c-Fos positive), TH-positive neurons in the ATAC-targeted SNc/VTA after treatment with CNO, compared with contralateral control ($P = 1.1 \times 10^{-3}$, paired two-tailed t-test, $n = 5$ mice; **$P < 0.01$; bars represent mean ± s.e.m), together with representative histology images of the targeted and contralateral brain regions stained for c-Fos (yellow), TH (blue) and hM3Dq-mCherry (red). Scale bars, 100 μm.

site of FUS-BBBO and the contralateral region. Among TH-positive neurons, we found a 7.3-fold increase in activation on the side of the brain targeted by the ATAC treatment after CNO administration (Fig. 6f, $n = 5$ mice, $P = 0.0011$, paired two-tailed t-test). Since ligand-independent activity of DREADDs has recently been shown to be present in peripheral neurons[53], we also tested c-Fos accumulation in the absence of CNO to evaluate this possibility in our experiments. We found no activation after saline administration (Supplementary Fig. 6, $n = 4$, $P = 0.26$, paired two-tailed t-test).

These results demonstrate spatially selective, CNO-dependent, intersectional neuromodulation in a Cre mouse line.

Tolerability of ATAC by brain tissue. Finally, to confirm that ATAC treatment is well tolerated by brain tissue, we examined hematoxylin-stained brain sections from 14 mice with a total of 84 FUS-BBBO sites. Consistent with previous findings[54], the majority of these sites (71.4%) had normal histology (Supplementary Fig. 7a,b). In the remaining FUS-targeted sites, we found small areas of apparent tissue damage with mean dimensions of 115 μm × 265 μm, which were not visible on sections ± 300 μm away from the site (Supplementary Fig. 7b,c). The average calculated volume of these features was 0.0027 ± 0.0007 mm³. This represents less than 0.1% of the typical FUS-BBBO site, which has a volume of 2.81 ± 0.51 mm³ (average of $n = 7$ sites quantified by MRI), and 0.01% of the mouse hippocampus (volume of 26 mm³)[55]. By comparison, the volume of brain displaced during invasive viral injections using typical needle gauges (27–33 gauge) is 0.1–0.4 mm³ (Supplementary Fig. 7d), resulting in damage still present seven weeks after the injection (Supplementary Fig. 7e). These results are consistent with the normal performance of ATAC-treated mice in behavioural tests and the ability of ATAC-treated regions to become chemogenetically activated and express c-Fos. In future translational studies, this safety profile could be further improved with feedback-controlled FUS-BBBO[56].

Discussion

Taken together, our results establish ATAC as a paradigm for non-invasive neuromodulation with a unique combination of spatial, cell-type and temporal specificity. This paradigm holds several advantages over existing techniques for both research and potential clinical applications. Compared with intracranial injections for viral gene delivery, which are invasive and often require multiple brain penetrations to cover the desired area (up to dozens in larger species[57,58]), FUS-BBBO enables comprehensive transduction of an entire brain region in a single session with relatively minimal tissue disruption and can more easily be scaled to larger animals and humans. Unlike optogenetics or electrical stimulators, ATAC can achieve neuromodulation non-invasively, without the need for permanently attached or implanted devices for chronic use. Since AAVs are being investigated in clinical trials with promising results[24–26,56], and FUS-BBBO has also been tested in the clinic[10], ATAC could become clinically relevant. While recent developments in AAV vectors also enable some variants to cross the BBB on their own[40], they do so without spatial selectivity.

Compared with emerging ultrasonic neuromodulation techniques in which ultrasound directly activates or inhibits brain regions or locally delivers neuromodulatory compounds[60–68], ATAC does not require an ultrasound transducer to be mounted on the subject during modulation. After transduction and expression of chemogenetic receptors in a genetically defined subset of cells at the FUS-targeted site, neuromodulation is conveniently controlled using a systemically bioavailable drug. The fact that a single FUS-BBBO session is required should also minimize the potential for non-specific cellular-level effects after multiple FUS-BBBO treatments[69,70].

In our behavioural proof of concept, a single injection of CNO several weeks after the FUS-BBBO procedure resulted in a 2.4-fold reduction in fear memory formation without any effects on normal exploratory behaviour. In addition, both the cell types modulated in the chosen brain region and the polarity of the modulation can be chosen precisely using cell-type-specific promoters and excitatory or inhibitory receptors. Finally, we showed that ATAC is compatible with intersectional genetic targeting in transgenic animals, making it potentially useful in a wide variety of basic and disease model studies.

The ATAC paradigm could be made more powerful with improvements in each of its components: FUS-BBBO, AAV vectors, cell type-specific promoters, chemogenetic receptors and ligands. For example, the incidence of FUS-induced lesions can be reduced through real-time monitoring of bubble cavitation to maximize molecular delivery while minimizing the possibility of damage[56,71–73]. The use of phased array transducers and protocols correcting skull-induced aberrations in the ultrasound field[20,74–77] could facilitate the scaling of ATAC to larger animals. At the same time, larger ultrasound transducer apertures (lower f-numbers) could reduce the focal zone size to make targeting more precise, while pulse sequences using chirps and random-based coded ultrasonic excitation[78] could reduce reverberations[79,80] within the brains of smaller animals. Finally, in research applications, FUS devices that perform targeting on the basis of stereotaxic coordinates rather than MRI guidance should make ATAC accessible to a broader range of neuroscience laboratories.

Additional work is also needed to make AAV vectors more efficient to reduce their required dose, and to make compact cell-type-specific promoters that work robustly in primates[28]. Finally, there are ongoing studies of the pharmacokinetics of chemogenetic ligands and receptors. It has recently been shown that CNO is metabolized to clozapine, which then activates DREADDs with high affinity[81]. Such studies highlight the need for continued optimization of ligands and their dosing for DREADD activation, and motivate the use of alternative ligands[82] and chemogenetic receptors[83,84], especially in species where metabolism of CNO to clozapine is significant. These improvements will facilitate the development and translation of ATAC as a paradigm for precise non-invasive control of neural circuits.

Methods

Animals. C57BL/6J mice were obtained from Jackson Lab. Transgenic TH-Cre mice were obtained from an internal colony at the California Institute of Technology and were originally generated[48] at Uppsala University. Animals were housed in a 12 h light/dark cycle and were provided with water and food ad libitum. All experiments were conducted under a protocol approved by the Institutional Animal Care and Use Committee of the California Institute of Technology.

FUS-BBBO. Male, 13–18-week-old C57BL/6J mice were anaesthetized with 2% isoflurane in air, the hair on their head removed with Nair depilation cream and then cannulated in the tail vein using a 30 gauge needle connected to PE10 tubing. The cannula was then flushed with 10 units (U) ml^{-1} of heparin in sterile saline (0.9% NaCl) and affixed to the mouse tail using tissue glue. Subsequently, the mice were placed in the custom-made plastic head mount and imaged in a 7 T MRI (Bruke Biospec). A fast low-angle shot sequence (echo time TE = 3.9 ms, repetition time TR = 15 ms, flip angle 20°) was used to record the position of the ultrasound transducer in relation to the mouse brain. Subsequently, the mice were injected via tail vein with AAV9 (1×10^{10} viral particles per g) encoding DREADDs in plasmids containing inverted terminal repeats of AAV (pAAV): pAAV-CaMKIIa-hM4Di-mCherry (Addgene plasmid no. 50477) or pAAV-CaMKIIa-hM3Dq-mCherry (Addgene plasmid no. 50476), both plasmids a gift from B. Roth (University of North Carolina). Immediately after viral injection, the mice were also injected with approximately 1.5×10^6 DEFINITY microbubbles (Lantheus) and 0.125 µmol of ProHance (Bracco Imaging) dissolved in sterile saline, per g of body weight. The dose of DEFINITY was optimized through preliminary studies from a starting point obtained from the literature[85]. The dose of ProHance was chosen on the basis of the manufacturer's recommendations. Within 30 s, the mice were insonated using an eight-channel FUS system (Image Guided Therapy) driving an eight-element annular array transducer with a diameter of 25 mm and a natural focal point of 20 mm, coupled to the head via Aquasonic gel. Gel was placed on the top and both sides of the animal's head to minimize reverberations from tissue/air interfaces. The focal distance was adjusted electronically, as shown in Supplementary Fig. 8, to target specific brain regions. The ultrasound parameters used were 1.5 MHz, 1% duty cycle and 1 Hz pulse repetition frequency for 120 pulses and were derived from a published protocol[17]. The pressure was calibrated using a fibre optic hydrophone (Precision Acoustics), with 21 measurements and an uncertainty of ± 3.8% (s.e.m.). The pressure for FUS-BBBO was chosen on the basis of multiple studies[17,86] and preliminary experiments in our lab. The ultrasound parameters were 1.5 MHz, 0.42 MPa pressure accounting for skull attenuation (18%)[23], 1% duty cycle and 1 Hz pulse repetition frequency for 120 pulses. For each FUS site, DEFINITY and ProHance were re-injected before

insonation. After FUS-BBBO, the mice were imaged again using the same fast low-angle shot sequence to confirm opening of the BBB and appropriate targeting. Immediately afterwards, the mice were placed in the home cage for recovery. The TH-Cre animals, all aged 18 weeks, were subjected to FUS-BBBO using the same protocol and using the same dose of AAV9 as for the C57BL/6J mice. All the TH-Cre animals were females.

MRI images were analysed using the ImageJ 'measurement' function. To estimate the size of the BBBO, we used a single FUS beam using standard parameters. The hyperintense area from ProHance extravasation was delineated manually, and the dimensions of the minor and major axes were recorded for $n = 7$ animals. The volumes were calculated assuming an ellipsoid shape. For the MRI intensity calculation, the four sites of FUS-BBBO in the dorsal hippocampus were delineated manually, and average signal intensity was calculated within the region for each mouse. The result was then divided by a mean signal intensity in an untargeted thalamus 1.5–2 mm below the hippocampus. The result was then compared with the size of an ultrasound beam.

Intracranial injection. Solutions of AAV9 encoding hM4Di-mCherry under a CaMKIIa promoter were injected into the hippocampus of male C57BL/6J mice (Jackson Lab) at 18 weeks of age using a NanoFil blunt-end 33 g needle coupled with a motorized pump (World Precision Instruments) at 100 nl min^{-1} using a stereotaxic frame (Kopf). The coordinates of the two pairs of sites with respect to the bregma were −2.2 mm anterior–posterior, ± 2 mm medio-lateral, −1.7 mm dorso-ventral and −3.2 mm anterior–posterior, ± 3.5 mm medio-lateral and −3 mm dorso-ventral. The needles remained in place after injection for 5 min to avoid backflow along the needle tract. The total volume of injection used was 500 nl. The total viral load was 5×10^8 in 0.5 µl per site, following previously published dosing[41], and seven weeks was allowed for expression to match the timeline used for analysis of expression and damage following FUS-BBBO.

c-Fos activation and immunostaining. C57BL/6J male mice of 13 weeks of age underwent FUS-BBBO to administer AAV9 carrying hM3Dq-mCherry into the hippocampus. Subsequently, the mice were housed singly to reduce background c-Fos expression. After 22 weeks of expression, the mice received an i.p. injection of 1 mg per kg CNO in sterile saline and were returned to the home cages. After 150 min, the mice were anaesthetized using ketamine/xylazine solution (80 mg per kg and 10 mg per kg, respectively, in PBS buffer) and perfused with cold PBS/heparin (10 U ml^{-1}), and immediately afterwards with 10% neutral buffered formalin. Their brains were extracted and postfixed in 10% neutral buffered formalin for at least 24 h. Brain sections (50 µm) were obtained using a VF-300 Compresstome (Precisionary Instruments). Subsequently, sections were blocked in 10% normal donkey serum and 0.2% Triton-X solution in PBS for 1 h at room temperature, and immunostaining with the primary antibody was performed using a goat anti-c-Fos antibody (SC-253-G, Santa Cruz Biotechnology) in 10% normal donkey serum and 0.2% Triton-X overnight at 4 °C. Afterwards, the sections were washed three times in PBS and incubated with a secondary donkey anti-goat antibody conjugated to Alexa Fluor 488 (A-11055, ThermoFisher). For activation of the hippocampus, the histological evaluation was performed by an observer blinded to the identity (hM3Dq positive or negative) of granular-layer nuclei in dorsal CA3. The expression status of the neurons was determined after the scoring of c-Fos expression. The cells were counterstained using TO-PRO-3 (ThermoFisher). The activation of TH neurons was evaluated by an observer blinded to the presence of FUS-BBBO targeting at a given site. TH-Cre mice expressed hM3Dq for nine weeks after FUS-BBBO, and were then given 1 mg per kg CNO. After 2 h, they were anaesthetized with ketamine/xylazine (80/10 mg per kg in PBS) and perfused using cold PBS/heparin (10 U ml^{-1}) and then 10% neutral buffered formalin. At least two sections per animal were used for c-Fos immunostaining of hM3Dq activation experiments, and all of the pyramidal neurons (for hippocampus experiments) or TH cells (for intersectional ATAC experiments) within each section were used for analysis. The saline control of c-Fos activation experiments in intersectional ATAC used one section per mouse, and all TH cells within each section were used for analysis. A three-dimensional reference atlas[87] was used to choose the appropriate regions and brain sections for each mouse and contralateral and ipsilateral controls to ascertain consistency in the choice of analysed sections. One region of interest in one out of six TH-Cre mice was damaged during sectioning, and the mouse could not be included in c-Fos evaluation. The time points for c-Fos testing were chosen on the basis of previous literature[88,89].

Gene expression evaluation. The gene expression timeline was chosen on the basis of previous studies indicating that the expression of genes delivered with AAV9 is stable after six weeks[90] and showing activity of DREADDs after that time point[91,92]. In addition, the long-term expression of 22 weeks in Fig. 4 was chosen to establish whether DREADDs remain active after a longer period of time following FUS-BBBO delivery. To visualize DREADD expression across brain regions, we used immunostaining with a polyclonal rabbit anti-mCherry antibody (PA534974, ThermoFisher), a polyclonal goat anti-CaMKIIa antibody (PA519128, ThermoFisher) and a polyclonal goat anti-Gad67 (103220-296, LifeSpan) antibody in 10% normal donkey serum (D9663-10ML, Sigma-Aldrich) and 0.2% Triton-X in

PBS overnight at 4 °C. The TH expression was evaluated using an anti-TH chicken antibody (TYH, Aves Labs) incubated in normal goat serum (NS02L-1ML, Sigma-Aldrich) and 0.2% Triton-X in PBS overnight at 4 °C. The expression of protein gene product (PGP) 9.5 was evaluated using rabbit anti-PGP9.5 (ab10404, Abcam), incubated in 0.2% Triton-X in PBS overnight at 4 °C. Secondary antibodies were donkey anti-rabbit conjugated to DyLight 650 (84546, ThermoFisher), donkey anti-goat conjugated to DyLight 488 (SA5-10086, ThermoFisher) and goat anti-chicken conjugated to Alexa Fluor 488 (A-11039, ThermoFisher). Secondary antibodies were incubated in 10% normal donkey serum / 0.2% Triton-X in PBS for 4 h at room temperature. For quantitative comparison of expression levels between various regions of the hippocampus, we used mCherry fluorescence localized to cytoplasmic compartments and counted the number of cells in the pyramidal layers of the hippocampus showing detectable fluorescence. Cells were co-stained with a nuclear stain (4,6-diamidino-2-phenylindole (DAPI)) to allow delineation of nuclei and surrounding cytoplasmic regions. Cells that showed mCherry fluorescence surrounding the nucleus for at least 50% of its circumference were counted as positive to allow for a consistent comparison of expression between different hippocampal regions and conditions. The non-cytoplasmic localization of DREADD-mCherry necessitated the selection of this threshold. All the images were background normalized to allow for comparable evaluation of expression. Sections were obtained at 50 μm serially, in order. All sections were inspected for expression at a low-power fluorescent microscope, and representative sections were then imaged on a confocal microscope. Expression was evaluated for 3–5 sections per animal, and cells from each subfield of the hippocampus were added for each animal and normalized by the number of DAPI stained cells in the granular cell layer of that subfield. The interexperimenter variability was determined for two different researchers (B.L., J.O.S.) for $n = 6$ samples, with the difference in means smaller than 2.5% (mean = 42.5% versus mean = 41.5%, $P = 0.92$, heteroscedastic two-tailed t-test).

Behavioural testing. Behavioural studies for fear conditioning were performed in sound-attenuated fear conditioning chambers (30 cm × 25 cm × 25 cm, Med Associates). Animals were trained and tested for contextual fear in context A, which comprised a staggered wire grid floor, white light, 5% acetic acid for scent and no background noise. Locomotor testing was performed in context B, which was differentiated from context A by chamber shape, floor, illumination, odour, background noise and room location. Animal activity was recorded and quantified using Video Freeze software (Med Associates). For cued training, the tone was 80 dB and 30 s.

Fear conditioning. Mice were injected with CNO (10 mg per kg, i.p.) or equivalent volume of saline (i.p.) and, after 40–60 min, underwent contextual and cued fear conditioning in context A. This timeframe was chosen to allow CNO to reach its pharmacokinetic peak[93]. An initial baseline period of 3 min was followed by 3 × 30 s presentations of a tone co-terminated with a 2 s foot shock (0.7 mA), with an intertrial interval of 60 s. After the trials, the mice remained in the context for an additional 60 s, after which they were transported back into the vivarium. After 24 h, the mice were placed in context A to record contextual fear for the duration of the training (8 min and 40 s).

Exploratory behaviour analysis. Between 30 min and 45 min after the contextual fear test, the mice were transported to another room, placed in context B and allowed to explore the chamber for 3 min while their activity was recorded. Due to automated data acquisition and evaluation, no blinding was necessary.

Fear conditioning analysis. The mice were recorded using automated near-infrared video tracking in the fear conditioning chamber using the Video Freeze software. Mouse motion was measured using the activity score, from a video recording at 30 frames per second, with the motion threshold set at 18 activity units (the standard value in the software). Freezing was defined as an activity score below 18 units for at least 1 s. Average freezing in the context test was scored over the whole trial. Due to automated data acquisition and evaluation, no blinding was necessary.

Exclusions. Mice were excluded from the statistical analysis if their histologically determined DREADD expression was below 30% of cell bodies in the dorsal CA3 region of the hippocampus. This threshold was chosen on the basis of previous studies showing that behavioural effects generally require modulation of at least 30% of the neurons in a targeted region[94,95], and dorsal CA3 being the most robustly transfected hippocampus region. The resulting analysed groups had identical levels of expression (55.1% for the saline group and 60.5% for the CNO group, $P = 0.26$, heteroscedastic two-tailed t-test). In analyses including all mice, we found that DREADD expression in dorsal CA3 correlated with the formation of contextual fear memories in mice treated with CNO (coefficient of correlation $r = 0.62$, $n = 11$), but not in mice receiving saline ($r = 0.14$, $n = 14$) (Supplementary Fig. 9a). Even without excluding the four mice that had expression below 30%, a direct comparison between ATAC mice treated with CNO and saline showed a statistically significant reduction of contextual fear (53.2% versus 34%, $n = 13$ and $n = 11$, $P = 0.0193$, heteroscedastic two-tailed t-test). Variability in gene expression may have been due to variability in i.v. injections of virus during the FUS-BBBO procedure, since we found no difference between these mice in longitudinal

relaxation time (T_1)-weighted MRI signal enhancement post-FUS-BBBO (Supplementary Fig. 9b).

Statistical analysis. Data were analysed using either a two-tailed t-test with unequal variance (when two samples were compared and when data were deemed normal with a Shapiro–Wilk test) or one-way analysis of variance with a Tukey honestly significant difference post hoc test (when more than two samples were compared). All data with $P < 0.05$ were considered to be significant. All data were tested for normality using a Shapiro–Wilk test. Samples with two conditions and non-normal distributions were tested by a nonparametric test (Mann–Whitney). All central tendencies reported are averages.

Histological analysis. Analysis of the FUS-BBBO safety was performed using hematoxylin staining and autofluorescence. All of the vibratome sections (50 μm) within the hippocampus were imaged under a microscope with a ×10 objective to identify potential lesions ($n = 14$ mice). The sections showing the largest anomalies were then observed at a greater magnification (×20 objective). The FUS-induced lesions were autofluorescent, and fluorescence microscopy was used for measurements. The volumes were calculated assuming an ellipsoid shape of the damage, with maximum diameters within a section used for the major and minor axes. The volume of lesions was calculated using an ellipsoid volume formula (volume $v = 4/3 × \pi × (width/2)^2 × length/2$). To confirm the anatomy of the lesions, hematoxylin staining was performed: vibratome sections were stained for 30–45 s in 20% Gill no. 3 hematoxylin, followed by a brief wash in PBS and a 5 s dip in Rapid-Chrome blueing solution (ThermoFisher). Each section was then washed twice in PBS and mounted in a water-based medium (ProLong Gold, ThermoFisher).

Illustrations. The structure of AAV9[96] in Fig. 1 was rendered using QuteMol[97]. The three-dimensional rendering of the hippocampus in Fig. 2 was generated using the Rhinoceros software with models obtained from a three-dimensional brain atlas reconstructor[98] and a Waxholm space dataset[99].

Reporting Summary. Further information on experimental design is available in the Nature Research Reporting Summary linked to this article.

Data availability. The authors declare that all data supporting the findings of this study are available within the paper and its supplementary information. Raw data files are available from the corresponding author upon reasonable request.

References

1. Hirtz, D. et al. How common are the 'common' neurologic disorders? *Neurology* **68**, 326–337 (2007).
2. Pangalos, M. N., Schechter, L. E. & Hurko, O. Drug development for CNS disorders: strategies for balancing risk and reducing attrition. *Nat. Rev. Drug Discov.* **6**, 521–532 (2007).
3. *The Numbers Count: Mental Disorders in America* (National Institutes of Health, 2013).
4. Sakurai, T. The role of orexin in motivated behaviours. *Nat. Rev. Neurosci.* **15**, 719–731 (2014).
5. Russo, S. J. & Nestler, E. J. The brain reward circuitry in mood disorders. *Nat. Rev. Neurosci.* **14**, 609–625 (2013).
6. Apkarian, A. V., Hashmi, J. A. & Baliki, M. N. Pain and the brain: specificity and plasticity of the brain in clinical chronic pain. *Pain* **152**, S49–S64 (2011).
7. Shin, L. M. & Liberzon, I. The neurocircuitry of fear, stress, and anxiety disorders. *Neuropsychopharmacology* **35**, 169–191 (2009).
8. Koob, G. F. & Volkow, N. D. Neurocircuitry of addiction. *Neuropsychopharmacology* **35**, 217–238 (2009).
9. Burnett, C. J. & Krashes, M. J. Resolving behavioral output via chemogenetic designer receptors exclusively activated by designer drugs. *J. Neurosci.* **36**, 9268–9282 (2016).
10. Carpentier, A. et al. Clinical trial of blood–brain barrier disruption by pulsed ultrasound. *Sci. Transl. Med.* **8**, 343re2 (2016).
11. Elias, W. J. et al. A randomized trial of focused ultrasound thalamotomy for essential tremor. *New Engl. J. Med.* **375**, 730–739 (2016).
12. Dobrakowski, P. P. et al. MR-guided focused ultrasound: a new generation treatment of Parkinson's disease, essential tremor and neuropathic pain. *Interv. Neuroradiol.* **20**, 275–282 (2014).
13. Hynynen, K., McDannold, N., Vykhodtseva, N. & Jolesz, F. A. Noninvasive MR imaging-guided focal opening of the blood–brain barrier in rabbits. *Radiology* **220**, 640–646 (2001).
14. Tung, Y. S., Vlachos, F., Feshitan, J. A., Borden, M. A. & Konofagou, E. E. The mechanism of interaction between focused ultrasound and microbubbles in blood–brain barrier opening in mice. *J. Acoust. Soc. Am.* **130**, 3059–3067 (2011).

15. Samiotaki, G., Acosta, C., Wang, S. & Konofagou, E. E. Enhanced delivery and bioactivity of the neurturin neurotrophic factor through focused ultrasound-mediated blood–brain barrier opening in vivo. *J. Cereb. Blood Flow Metab.* **35**, 611–622 (2015).

16. O'Reilly, M. A. & Hynynen, K. Ultrasound enhanced drug delivery to the brain and central nervous system. *Int. J. Hyperth.* **28**, 386–396 (2012).

17. Thevenot, E. et al. Targeted delivery of self-complementary adeno-associated virus serotype 9 to the brain, using magnetic resonance imaging-guided focused ultrasound. *Human Gene Ther.* **23**, 1144–1155 (2012).

18. Wang, S., Olumolade, O. O., Sun, T., Samiotaki, G. & Konofagou, E. E. Non-invasive, neuron-specific gene therapy can be facilitated by focused ultrasound and recombinant adeno-associated virus. *Gene Ther.* **22**, 104–110 (2015).

19. Nance, E. et al. Non-invasive delivery of stealth, brain-penetrating nanoparticles across the blood–brain barrier using MRI-guided focused ultrasound. *J. Control. Release* **189**, 123–132 (2014).

20. Clement, G. T. & Hynynen, K. A non-invasive method for focusing ultrasound through the human skull. *Phys. Med. Biol.* **47**, 1219–1236 (2002).

21. Hsu, P. H. et al. Noninvasive and targeted gene delivery into the brain using microbubble-facilitated focused ultrasound. *PLoS ONE* **8**, e57682 (2013).

22. Treat, L. H. et al. Targeted delivery of doxorubicin to the rat brain at therapeutic levels using MRI-guided focused ultrasound. *Int. J. Cancer* **121**, 901–907 (2007).

23. Choi, J. J., Pernot, M., Small, S. A. & Konofagou, E. E. Noninvasive, transcranial and localized opening of the blood–brain barrier using focused ultrasound in mice. *Ultrasound Med. Biol.* **33**, 95–104 (2007).

24. Ginn, S. L., Alexander, I. E., Edelstein, M. L., Abedi, M. R. & Wixon, J. Gene therapy clinical trials worldwide to 2012—an update. *J. Gene Med.* **15**, 65–77 (2013).

25. Mendell, J. R. et al. Single-dose gene-replacement therapy for spinal muscular atrophy. *New Engl. J. Med.* **377**, 1713–1722 (2017).

26. Rangarajan, S. et al. AAV5–factor VIII gene transfer in severe hemophilia A. *New Engl. J. Med.* **377**, 2519–2530 (2017).

27. Bender, E. Gene therapy: industrial strength. *Nature* **537**, S57–S59 (2016).

28. Kotterman, M. A., Chalberg, T. W. & Schaffer, D. V. Viral vectors for gene therapy: translational and clinical outlook. *Annu. Rev. Biomed. Eng.* **17**, 63–89 (2015).

29. Luo, L., Callaway, E. M. & Svoboda, K. Genetic dissection of neural circuits. *Neuron* **57**, 634–660 (2008).

30. Alonso, A. et al. Focal delivery of AAV2/1-transgenes into the rat brain by localized ultrasound-induced BBB opening. *Mol. Ther. Nucleic Acids* **2**, e73 (2013).

31. Sternson, S. M. & Roth, B. L. Chemogenetic tools to interrogate brain functions. *Annu. Rev. Neurosci.* **37**, 387–407 (2014).

32. Shapiro, M. G., Frazier, S. J. & Lester, H. A. Unparalleled control of neural activity using orthogonal pharmacogenetics. *ACS Chem. Neurosci.* **3**, 619–629 (2012).

33. English, J. G. & Roth, B. L. Chemogenetics—a transformational and translational platform. *JAMA Neurol.* **72**, 1361–1366 (2015).

34. Smith, K. S., Bucci, D. J., Luikart, B. W. & Mahler, S. V. DREADDs: use and application in behavioral neuroscience. *Behav. Neurosci.* **130**, 137–155 (2016).

35. Armbruster, B. N., Li, X., Pausch, M. H., Herlitze, S. & Roth, B. L. Evolving the lock to fit the key to create a family of G protein-coupled receptors potently activated by an inert ligand. *Proc. Natl Acad. Sci. USA* **104**, 5163–5168 (2007).

36. Andersen, P. et al. (eds) *The Hippocampus Book* (Oxford Univ. Press, Oxford, 2007).

37. Castle, M. J., Turunen, H. T., Vandenberghe, L. H. & Wolfe, J. H. Controlling AAV tropism in the nervous system with natural and engineered capsids. *Methods Mol. Biol.* **1382**, 133–149 (2016).

38. Dittgen, T. et al. Lentivirus-based genetic manipulations of cortical neurons and their optical and electrophysiological monitoring in vivo. *Proc. Natl Acad. Sci. USA* **101**, 18206–18211 (2004).

39. Chan, K. Y. et al. Engineered AAVs for efficient noninvasive gene delivery to the central and peripheral nervous systems. *Nat. Neurosci.* **20**, 1172–1179 (2017).

40. Deverman, B. E. et al. Cre-dependent selection yields AAV variants for widespread gene transfer to the adult brain. *Nat. Biotechnol.* **34**, 204–209 (2016).

41. Zhu, H. et al. Chemogenetic inactivation of ventral hippocampal glutamatergic neurons disrupts consolidation of contextual fear memory. *Neuropsychopharmacology* **39**, 1880–1892 (2014).

42. Whitaker, A. M., Gilpin, N. W. & Edwards, S. Animal models of post-traumatic stress disorder and recent neurobiological insights. *Behav. Pharmacol.* **25**, 398–409 (2014).

43. VanElzakker, M. B., Dahlgren, M. K., Davis, F. C., Dubois, S. & Shin, L. M. From Pavlov to PTSD: the extinction of conditioned fear in rodents, humans, and anxiety disorders. *Neurobiol. Learn. Mem.* **113**, 3–18 (2014).

44. Kheirbek, M. A. et al. Differential control of learning and anxiety along the dorsoventral axis of the dentate gyrus. *Neuron* **77**, 955–968 (2013).

45. Blanchard, D. C. & Blanchard, R. J. Ethoexperimental approaches to the biology of emotion. *Annu. Rev. Psychol.* **39**, 43–68 (1988).

46. Burgess, A., Dubey, S., Nhan, T., Aubert, I. & Hynynen, K. Therapeutic effects of focused ultrasound-mediated blood–brain barrier opening in a mouse model of Alzheimer's disease. *J. Ther. Ultrasound* **3**, O16 (2015).

47. Mooney, S. J. et al. Focused ultrasound-induced neurogenesis requires an increase in blood–brain barrier permeability. *PLoS ONE* **11**, e0159892 (2016).

48. Lindeberg, J. et al. Transgenic expression of Cre recombinase from the tyrosine hydroxylase locus. *Genesis* **40**, 67–73 (2004).

49. Jagmag, S. A., Tripathi, N., Shukla, S. D., Maiti, S. & Khurana, S. Evaluation of models of Parkinson's disease. *Front. Neurosci.* **9**, 503 (2015).

50. Lammel, S., Lim, B. K. & Malenka, R. C. Reward and aversion in a heterogeneous midbrain dopamine system. *Neuropharmacology* **76** (Part B), 351–359 (2014).

51. Chen, R., Romero, G., Christiansen, M. G., Mohr, A. & Anikeeva, P. Wireless magnetothermal deep brain stimulation. *Science* **347**, 1477–1480 (2015).

52. Atasoy, D., Aponte, Y., Su, H. H. & Sternson, S. M. A FLEX switch targets Channelrhodopsin-2 to multiple cell types for imaging and long-range circuit mapping. *J. Neurosci.* **28**, 7025–7030 (2008).

53. Saloman, J. L. et al. Gi-DREADD expression in peripheral nerves produces ligand-dependent analgesia, as well as ligand-independent functional changes in sensory neurons. *J. Neurosci.* **36**, 10769–10781 (2016).

54. Baseri, B., Choi, J. J., Tung, Y. S. & Konofagou, E. E. Multi-modality safety assessment of blood–brain barrier opening using focused ultrasound and DEFINITY microbubbles: a short-term study. *Ultrasound Med. Biol.* **36**, 1445–1459 (2010).

55. Badea, A., Ali-Sharief, A. A. & Johnson, G. A. Morphometric analysis of the C57BL/6J mouse brain. *NeuroImage* **37**, 683–693 (2007).

56. Tung, Y. S. et al. In vivo transcranial cavitation threshold detection during ultrasound-induced blood–brain barrier opening in mice. *Phys. Med. Biol.* **55**, 6141–6155 (2010).

57. Eldridge, M. A. G. et al. Chemogenetic disconnection of monkey orbitofrontal and rhinal cortex reversibly disrupts reward value. *Nat. Neurosci.* **19**, 37–39 (2015).

58. Thomsen, G. M. et al. Delayed disease onset and extended survival in the SOD1^{G93A} rat model of amyotrophic lateral sclerosis after suppression of mutant SOD1 in the motor cortex. *J. Neurosci.* **34**, 15587–15600 (2014).

59. Russell, S. et al. Efficacy and safety of voretigene neparvovec (AAV2-hRPE65v2) in patients with RPE65-mediated inherited retinal dystrophy: a randomised, controlled, open-label, phase 3 trial. *Lancet* **390**, 849–860 (2017).

60. Tufail, Y. et al. Transcranial pulsed ultrasound stimulates intact brain circuits. *Neuron* **66**, 681–694 (2010).

61. King, R. L., Brown, J. R., Newsome, W. T. & Pauly, K. B. Effective parameters for ultrasound-induced in vivo neurostimulation. *Ultrasound Med. Biol.* **39**, 312–331 (2013).

62. Deffieux, T. et al. Low-intensity focused ultrasound modulates monkey visuomotor behavior. *Curr. Biol.* **23**, 2430–2433 (2013).

63. Landhuis, E. Ultrasound for the brain. *Nature* **551**, 257–259 (2017).

64. Airan, R. D. et al. Noninvasive targeted transcranial neuromodulation via focused ultrasound gated drug release from nanoemulsions. *Nano Lett.* **17**, 652–659 (2017).

65. Sato, T., Shapiro, M. & Tsao, D. Ultrasonic neuromodulation causes widespread cortical activation via an indirect auditory mechanism. *Neuron* **98**, 1031–1041 (2018).

66. McDannold, N. et al. Targeted, noninvasive blockade of cortical neuronal activity. *Sci. Rep.* **5**, 16253 (2015).

67. Mehić, E. et al. Increased anatomical specificity of neuromodulation via modulated focused ultrasound. *PLoS ONE* **9**, e86939 (2014).

68. Tyler, W. J., Lani, S. W. & Hwang, G. M. Ultrasonic modulation of neural circuit activity. *Curr. Opin. Neurobiol.* **50**, 222–231 (2018).

69. Leinenga, G. & Gotz, J. Scanning ultrasound removes amyloid-β and restores memory in an Alzheimer's disease mouse model. *Sci. Transl. Med.* **7**, 278ra233 (2015).

70. Burgess, A. et al. Alzheimer disease in a mouse model: MR imaging-guided focused ultrasound targeted to the hippocampus opens the blood–brain barrier and improves pathologic abnormalities and behavior. *Radiology* **273**, 736–745 (2014).

71. Burgess, M. T., Apostolakis, I. & Konofagou, E. E. Power cavitation-guided blood–brain barrier opening with focused ultrasound and microbubbles. *Phys. Med. Biol.* **63**, 065009 (2018).

72. McDannold, N., Vykhodtseva, N. & Hynynen, K. Targeted disruption of the blood–brain barrier with focused ultrasound: association with cavitation activity. *Phys. Med. Biol.* **51**, 793–807 (2006).

73. Sun, T. et al. Acoustic cavitation-based monitoring of the reversibility and permeability of ultrasound-induced blood–brain barrier opening. *Phys. Med. Biol.* **60**, 9079–9094 (2015).

74. Jingfei, L., Josquin, F., Douglas, N. S., Olivier Le, B. & Katherine, W. F. Development of a spherically focused phased array transducer for ultrasonic image-guided hyperthermia. *Phys. Med. Biol.* **61**, 5275–5296 (2016).

75. Deng, L., O'Reilly, M. A., Jones, R. M., An, R. & Hynynen, K. A multi-frequency sparse hemispherical ultrasound phased array for microbubble-mediated transcranial therapy and simultaneous cavitation mapping. *Phys. Med. Biol.* **61**, 8476–8501 (2016).

76. Downs, M. E. et al. Long-term safety of repeated blood–brain barrier opening via focused ultrasound with microbubbles in non-human primates performing a cognitive task. *PLoS ONE* **10**, e0125911 (2015).

77. Pernot, M., Aubry, J. F., Tanter, M., Thomas, J. L. & Fink, M. High power transcranial beam steering for ultrasonic brain therapy. *Phys. Med. Biol.* **48**, 2577–2589 (2003).

78. Kamimura, H. A. S. et al. Chirp- and random-based coded ultrasonic excitation for localized blood–brain barrier opening. *Phys. Med. Biol.* **60**, 7695–7712 (2015).

79. O'Reilly, M. A., Huang, Y. & Hynynen, K. The impact of standing wave effects on transcranial focused ultrasound disruption of the blood–brain barrier in a rat model. *Phys. Med. Biol.* **55**, 5251–5267 (2010).

80. Younan, Y. et al. Influence of the pressure field distribution in transcranial ultrasonic neurostimulation. *Med. Phys.* **40**, 082902 (2016).

81. Gomez, J. L. et al. Chemogenetics revealed: DREADD occupancy and activation via converted clozapine. *Science* **357**, 503–507 (2017).

82. Roth, B. L. DREADDs for neuroscientists. *Neuron* **89**, 683–694 (2016).

83. Vardy, E. et al. A new DREADD facilitates the multiplexed chemogenetic interrogation of behavior. *Neuron* **86**, 936–946 (2015).

84. Magnus, C. J. et al. Chemical and genetic engineering of selective ion channel–ligand interactions. *Science* **333**, 1292–1296 (2011).

85. Wang, S., Samiotaki, G., Olumolade, O., Feshitan, J. A. & Konofagou, E. E. Microbubble type and distribution dependence of focused ultrasound-induced blood–brain barrier opening. *Ultrasound Med. Biol.* **40**, 130–137 (2014).

86. Choi, J. J., Selert, K., Vlachos, F., Wong, A. & Konofagou, E. E. Noninvasive and localized neuronal delivery using short ultrasonic pulses and microbubbles. *Proc. Natl Acad. Sci. USA* **108**, 16539–16544 (2011).

87. Lein, E. S. et al. Genome-wide atlas of gene expression in the adult mouse brain. *Nature* **445**, 168–176 (2007).

88. Grippo, R. M., Purohit, A. M., Zhang, Q., Zweifel, L. S. & Guler, A. D. Direct midbrain dopamine input to the suprachiasmatic nucleus accelerates circadian entrainment. *Curr. Biol.* **27**, 2465–2475 (2017).

89. Koch, M. et al. Hypothalamic POMC neurons promote cannabinoid-induced feeding. *Nature* **519**, 45–50 (2015).

90. Zincarelli, C., Soltys, S., Rengo, G. & Rabinowitz, J. E. Analysis of AAV serotypes 1–9 mediated gene expression and tropism in mice after systemic injection. *Mol. Ther.* **16**, 1073–1080 (2008).

91. Mahler, S. V. et al. Designer receptors show role for ventral pallidum input to ventral tegmental area in cocaine seeking. *Nat. Neurosci.* **17**, 577–585 (2014).

92. Eliava, M. et al. A new population of parvocellular oxytocin neurons controlling magnocellular neuron activity and inflammatory pain processing. *Neuron* **89**, 1291–1304 (2016).

93. Alexander, G. M. et al. Remote control of neuronal activity in transgenic mice expressing evolved G protein-coupled receptors. *Neuron* **63**, 27–39 (2009).

94. Sananbenesi, F. et al. A hippocampal Cdk5 pathway regulates extinction of contextual fear. *Nat. Neurosci.* **10**, 1012–1019 (2007).

95. Kim, K. M. et al. Optogenetic mimicry of the transient activation of dopamine neurons by natural reward is sufficient for operant reinforcement. *PLoS ONE* **7**, e33612 (2012).

96. DiMattia, M. A. et al. Structural insight into the unique properties of adeno-associated virus serotype 9. *J. Virol.* **86**, 6947–6958 (2012).

97. Tarini, M., Cignoni, P. & Montani, C. Ambient occlusion and edge cueing for enhancing real time molecular visualization. *IEEE Trans. Vis. Comput. Gr.* **12**, 1237–1244 (2006).

98. Majka, P., Kublik, E., Furga, G. & Wojcik, D. K. Common Atlas Format and 3D Brain Atlas Reconstructor: infrastructure for constructing 3D brain atlases. *Neuroinformatics* **10**, 181–197 (2012).

99. Johnson, G. A. et al. Waxholm space: an image-based reference for coordinating mouse brain research. *NeuroImage* **53**, 365–372 (2010).

Author contributions

J.O.S. and M.G.S. conceived and planned the research. J.O.S. performed the in vivo experiments. J.O.S., B.L., A.L.-G. and D.M. performed the histological experiments. J.O.S. and B.L. analysed the data. J.O.S. and M.G.S. wrote the manuscript with input from all other authors. M.G.S. supervised the research.

Competing interests

The authors declare no competing interests.

Additional information

Supplementary information is available for this paper at https://doi.org/10.1038/s41551-018-0258-2.

Reprints and permissions information is available at www.nature.com/reprints.

Correspondence and requests for materials should be addressed to M.G.S.

Publisher's note: Springer Nature remains neutral with regard to jurisdictional claims in published maps and institutional affiliations.

nature research

Corresponding author(s): Mikhail G. Shapiro

Reporting Summary

Nature Research wishes to improve the reproducibility of the work that we publish. This form provides structure for consistency and transparency in reporting. For further information on Nature Research policies, see Authors & Referees and the Editorial Policy Checklist.

Statistical parameters

When statistical analyses are reported, confirm that the following items are present in the relevant location (e.g. figure legend, table legend, main text, or Methods section).

n/a	Confirmed	
☐	☒	The exact sample size (*n*) for each experimental group/condition, given as a discrete number and unit of measurement
☐	☒	An indication of whether measurements were taken from distinct samples or whether the same sample was measured repeatedly
☐	☒	The statistical test(s) used AND whether they are one- or two-sided *Only common tests should be described solely by name; describe more complex techniques in the Methods section.*
☒	☐	A description of all covariates tested
☐	☒	A description of any assumptions or corrections, such as tests of normality and adjustment for multiple comparisons
☐	☒	A full description of the statistics including central tendency (e.g. means) or other basic estimates (e.g. regression coefficient) AND variation (e.g. standard deviation) or associated estimates of uncertainty (e.g. confidence intervals)
☐	☒	For null hypothesis testing, the test statistic (e.g. *F*, *t*, *r*) with confidence intervals, effect sizes, degrees of freedom and *P* value noted *Give P values as exact values whenever suitable.*
☒	☐	For Bayesian analysis, information on the choice of priors and Markov chain Monte Carlo settings
☒	☐	For hierarchical and complex designs, identification of the appropriate level for tests and full reporting of outcomes
☒	☐	Estimates of effect sizes (e.g. Cohen's *d*, Pearson's *r*), indicating how they were calculated
☐	☒	Clearly defined error bars *State explicitly what error bars represent (e.g. SD, SE, CI)*

Our web collection on statistics for biologists may be useful.

Software and code

Policy information about availability of computer code

Data collection	We used Video Freeze v2.0 (Med Associates) for video capture and behavioral analysis. We used ThermoGuide v3846 (Image Guided Therapy) and Paravision v5.1 (Bruker) for MRI-guided focused ultrasound and MRI image acquisition.
Data analysis	We used Excel 2013 (Microsoft), Prism v7 (Graphpad), ImageJ v1.50a (NIH) and Zen v2.3 (Zeiss) for data and image analysis and plotting. Illustrations were made in Illustrator CC (Adobe), QuteMol v.0.4.1 and Rhinoceros 3D v5.0 (McNeel).

For manuscripts utilizing custom algorithms or software that are central to the research but not yet described in published literature, software must be made available to editors/reviewers upon request. We strongly encourage code deposition in a community repository (e.g. GitHub). See the Nature Research guidelines for submitting code & software for further information.

Data

Policy information about availability of data

All manuscripts must include a data availability statement. This statement should provide the following information, where applicable:

- Accession codes, unique identifiers, or web links for publicly available datasets
- A list of figures that have associated raw data
- A description of any restrictions on data availability

The authors declare that all data supporting the findings of this study are available within the paper and its supplementary information. Raw data files are available from the corresponding author upon reasonable request.

Field-specific reporting

Please select the best fit for your research. If you are not sure, read the appropriate sections before making your selection.

☒ Life sciences ☐ Behavioural & social sciences ☐ Ecological, evolutionary & environmental sciences

For a reference copy of the document with all sections, see nature.com/authors/policies/ReportingSummary-flat.pdf

Life sciences study design

All studies must disclose on these points even when the disclosure is negative.

Sample size	Sample sizes were chosen on the basis of preliminary experiments so as to provide sufficient power for statistical comparison (where appropriate). Power analysis was not performed a priori.
Data exclusions	Exclusions were based on loss or damage of samples during tissue processing, or on the basis of lack of DREADD expression. Detailed descriptions can be found in Methods.
Replication	All replicates are reported in the manuscript.
Randomization	All groups were randomized. Mice were randomized with regard to their initial treatment (FUS-BBBO+AAV, AAV-only or no treatment) and to the administration of CNO or saline in behavioral and c-Fos experiments. The placement in specific fear-conditioning chambers was randomized for all groups.
Blinding	Data was blinded during histological analysis. Behavioral analyses were automated and required no blinding.

Reporting for specific materials, systems and methods

Materials & experimental systems

n/a	Involved in the study
☐	☒ Unique biological materials
☐	☒ Antibodies
☒	☐ Eukaryotic cell lines
☒	☐ Palaeontology
☐	☒ Animals and other organisms
☒	☐ Human research participants

Methods

n/a	Involved in the study
☒	☐ ChIP-seq
☒	☐ Flow cytometry
☐	☒ MRI-based neuroimaging

Unique biological materials

Policy information about availability of materials

Obtaining unique materials	AAV9 viruses used in this study can be purchased commercially (for example, from Addgene).

Antibodies

Antibodies used	All antibodies are commercially purchased and included: goat anti-c-Fos antibody (SC-253-G, SCBT, Santa Cruz, CA), polyclonal rabbit anti-mCherry antibody (PA534974, Thermofisher), a polyclonal goat anti-CaMKIIa antibody (PA519128, Thermofisher) and

a polyclonal goat anti-Gad67 (Lifespan, 103220-296), anti-TH chicken antibody (TYH, Aves lab), using rabbit anti-PGP9.5 (Abcam, ab10404). The secondary antibodies were: donkey anti-goat antibody conjugated to Alexa-488 (A-11055, Thermofisher), donkey anti-rabbit conjugated to Dylight-650 (#84546, ThermoFisher), donkey anti-goat conjugated to Dylight-488 (SA510086) and goat anti-chicken conjugated to Alexa 488 (A-11039, ThermoFisher).

Validation | Validated by the manufacturer.

Animals and other organisms

Policy information about studies involving animals; ARRIVE guidelines recommended for reporting animal research

Laboratory animals | C57BL6J mice were obtained from JAX laboratories, with ages 13–18 weeks at the start of experiments. Transgenic TH-CRE mice were obtained from a Caltech's internal colony, and were originally generated at Uppsala University, Sweden (ref. 49). Animals were housed in 12-hour light/dark cycles and were provided water and food ad libitum. All experiments were conducted under a protocol approved by the Institutional Animal Care and Use Committee of the California Institute of Technology.

Wild animals | The study did not involve wild animals.

Field-collected samples | The study did not involve samples collected from the field.

Magnetic resonance imaging

Experimental design

Design type | Static image

Design specifications | Single image

Behavioral performance measures | No behavioural performance was measured.

Acquisition

Imaging type(s) | FLASH

Field strength | 7T

Sequence & imaging parameters | Flash, 3D, coronal: 3.9 ms TE, 15ms TR, 15 deg. flip angle; Voxel size: 200x200x351 micrometres; matrix: 130x130x114
Flash, 2D, axial: 3ms TE, 100ms TR, 30 deg flip angle, voxel: 80x80x350 micrometres; matrix 225x225x8

Area of acquisition | Whole brains were scanned.

Diffusion MRI ☐ Used ☒ Not used

Preprocessing

Preprocessing software | No preprocessing was used.

Normalization | No normalization was used.

Normalization template | No template was used.

Noise and artifact removal | No noise removal or artifact removal were used.

Volume censoring | No volume censoring was used.

Statistical modeling & inference

Model type and settings | No statistical modeling was used.

Effect(s) tested | No statistical effects were tested.

Specify type of analysis: ☒ Whole brain ☐ ROI-based ☐ Both

Statistic type for inference (See Eklund et al. 2016) | None used.

Correction | None needed.

Models & analysis

n/a	Involved in the study
☒	Functional and/or effective connectivity
☒	Graph analysis
☒	Multivariate modeling or predictive analysis